Interface engineering of self-supported Ni_3S_2/MoS_2@MXene heterostructure on nickel foam for advanced asymmetric supercapacitor with superior energy density

Monika Patel[a], Riddhi Patel[a], Kajal Mahabari[a], Ranjit D Mohili[a], Arvind H. Jadhav[b], Mani Govindasamy[c,d] and Nitin Chaudhari*[a]

[a]Advanced Hybrid Nanomaterial Laboratory, Department of Chemistry, School of Energy Technology, Pandit Deendayal Energy University, Gandhinagar, 382426, Gujarat, India.
[b]Centre for Nano and Material Science (CNMS), Jain University, Jain Global Campus, Bangalore, 562112, Karnataka, India.
[c]International Ph.D. Program in Innovative Technology of Biomedical Engineering and Medical Devices, Ming Chi University of Technology, New Taipei City 24301, Taiwan.
[d]Centre for Applied Research, Saveetha School of Engineering, Saveetha Institute of Medical and Technical Sciences (SIMATS), Chennai, Tamil Nadu 602105, India.

*Corresponding author: nitin.chaudhari@sot.pdpu.ac.in

Characterization

The crystalline phases of the synthesized samples were analysed using X-ray diffraction (XRD) on a PANalytical X'Pert Powder diffractometer operated in Gonio mode with Cu $K\alpha_1$ radiation (λ = 1.5406 Å). Diffraction patterns were collected over a 2θ range of 5°–80°, using a step interval of 0.05° and a counting time of 0.5 s per step. The surface morphology and internal structure were examined using Transmission Electron Microscopy (TEM, JEOL JEM-2100) and Field Emission Scanning Electron Microscopy (FESEM, Zeiss Ultra 55), operated at 5 kV with a secondary electron detector. Elemental composition was determined via Energy Dispersive X-ray Spectroscopy (EDX) at accelerating voltages up to 15 kV. Raman spectroscopy (Jobin Yvon Horiba LABRAM-HR, 100–1000 nm range) was used for preliminary phase confirmation. The surface electronic structure and chemical states were further investigated using X-ray Photoelectron Spectroscopy (XPS, Thermo Scientific NEXSA) equipped with

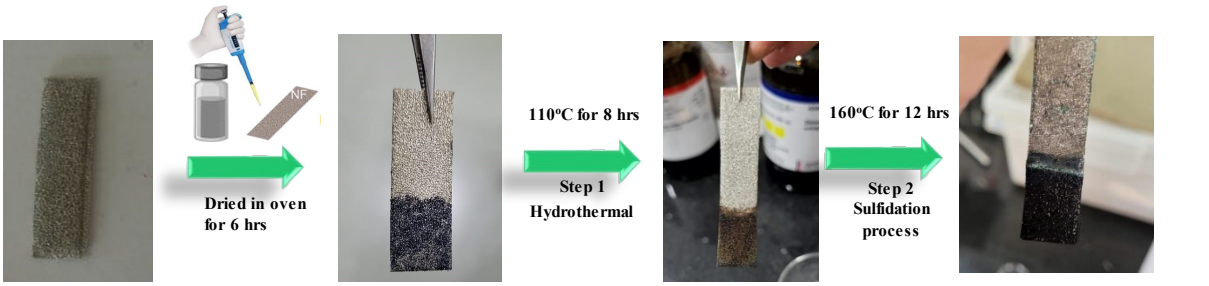

an Al Kα X-ray source (1486.6 eV) and a 400 µm beam spot.

Fig. S1. Images of pure Ni foam, MXene/NF, NiMo precursor@MXene/NF, and Ni_3S_2/MoS_2/NF, and Ni_3S_2/MoS_2@MXene/NF composites

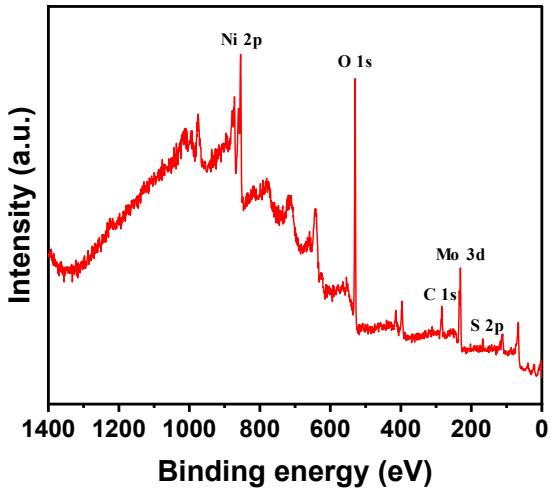

Fig. S2. (a) XPS survey spectrum of the Ni_3S_2/MoS_2@MXene/NF composites

Electrochemical measurement

The as-prepared Ni_3S_2/MoS_2@MXene/NF electrode was used directly without any binder, conductive additives, or additional processing for electrochemical evaluation. A three-electrode configuration was employed, with the hybrid electrode serving as the working electrode (mass loading was estimated to be approximately 4.0 mg), a platinum wire as the counter electrode, and an Ag/AgCl as the reference electrode. All measurements were performed in a 3 M KOH aqueous electrolyte. An asymmetric supercapacitor (ASC) device was assembled using the Ni_3S_2/MoS_2@MXene/NF electrode as the cathode and activated carbon as the anode. A gel electrolyte composed of 3M KOH with polyvinyl alcohol (PVA) was used, and a separator saturated in the gel was placed between the electrodes. The electrodes were cut into 16 mm diameter discs, coated with the active material slurry, and dried at 60 °C in a vacuum oven. The ASC device was assembled in a CR2032 coin-cell configuration and sealed using a hydraulic crimping machine under controlled pressure. To achieve proper charge balance between the cathode and anode, the mass ratio of both electrodes was calculated using the following relation [1] :

$$\frac{m_+}{m-} = \frac{C_- \times \Delta V_-}{C_+ \times \Delta V_+} \tag{1}$$

Where, C_+ and C_- are the specific capacitance (F g^{-1}), and ΔV_+ and ΔV_- are the operating voltage window (V) of the cathode and anode, respectively.

Electrochemical characterization was carried out in both three-electrode and two-electrode configurations using a 3M KOH electrolyte. The techniques employed included cyclic voltammetry (CV), galvanostatic charge-discharge (GCD), electrochemical impedance spectroscopy (EIS), cycling stability tests, and Ragone plot analysis to evaluate charge storage behaviour, rate capability, and energy density. The specific capacitance C (F g^{-1}) was calculated from CV and GCD curves using the following equations: [2]

From CV

$$C = \frac{1}{\Delta V}\int \frac{i_m dV}{v} \tag{2}$$

From GCD

$$C = \frac{i_m.\Delta t}{\Delta V} \tag{3}$$

Where i_m is the current density (A g^{-1}), Δt is the discharge time (s), ΔV is the voltage window (V)

Energy and power densities were calculated using the following relations:

$$E = \frac{1}{2 \times 3.6} C.\Delta V^2 \quad (4)$$

$$P = 3600 \times E/\Delta t \quad (5)$$

Where E is the energy density (Wh kg^{-1}), P is the power density (W kg^{-1}), C is the specific capacitance (F g^{-1}), ΔV is the voltage window (V), and Δt is the discharge time (s).

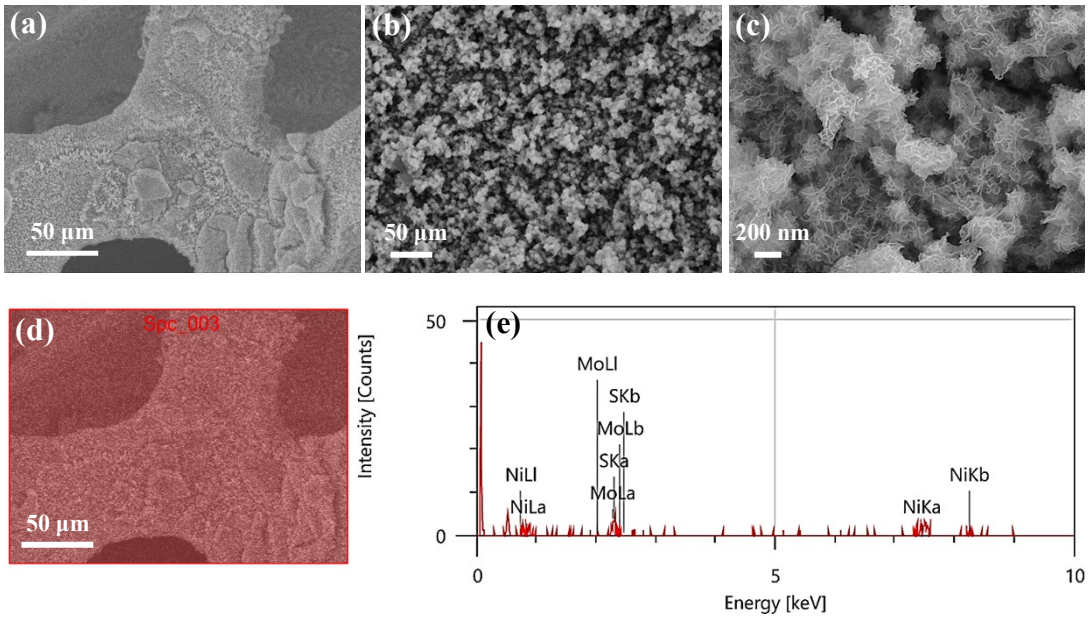

Fig. S3. (a-c) FESEM images of Ni_3S_2/MoS_2/NF hybrid electrode at different magnifications, showing a uniformly interconnected nanosheet architecture anchored on the MXene surface. (d) FESEM image showing the selected area used for EDX analysis. (e) EDX spectrum confirming the presence of Ni, Mo, and S elements, consistent with the formation of the Ni_3S_2/MoS_2/NF hybrid structure.

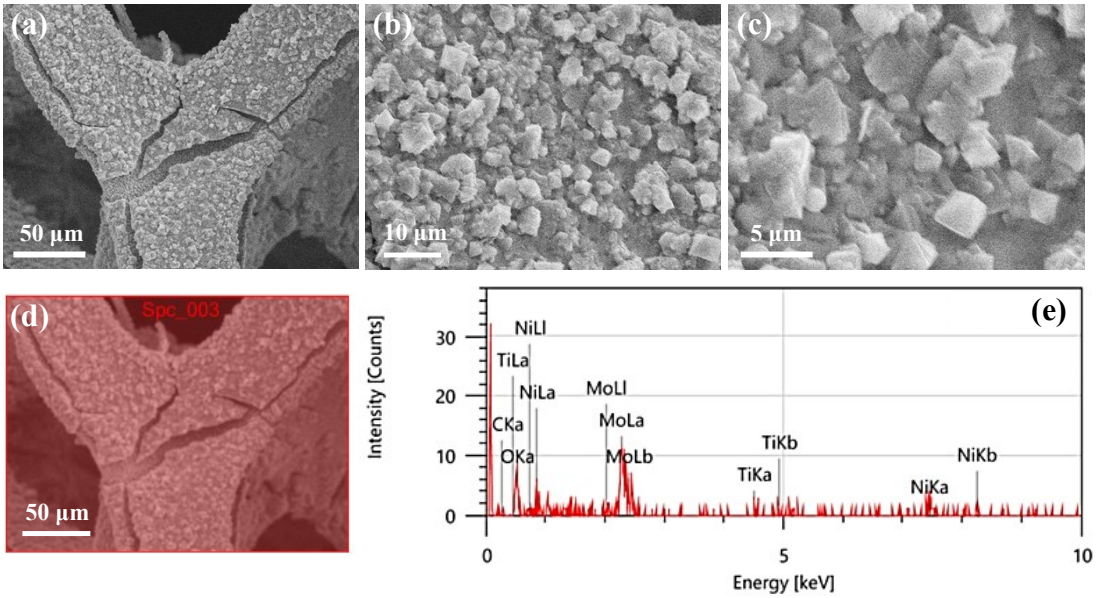

Fig. S4. (a-c) FESEM images of NiMo precursor@MXene/NF hybrid electrode at different magnifications, showing a uniformly interconnected octahedra firmly anchored on the MXene surface. (d) FESEM image showing the selected area used for EDX analysis. (e) EDX spectrum further confirming the presence of Ni, Mo, Ti and C elements, consistent with the formation of the NiMo precursor@MXene/NF hybrid structure.

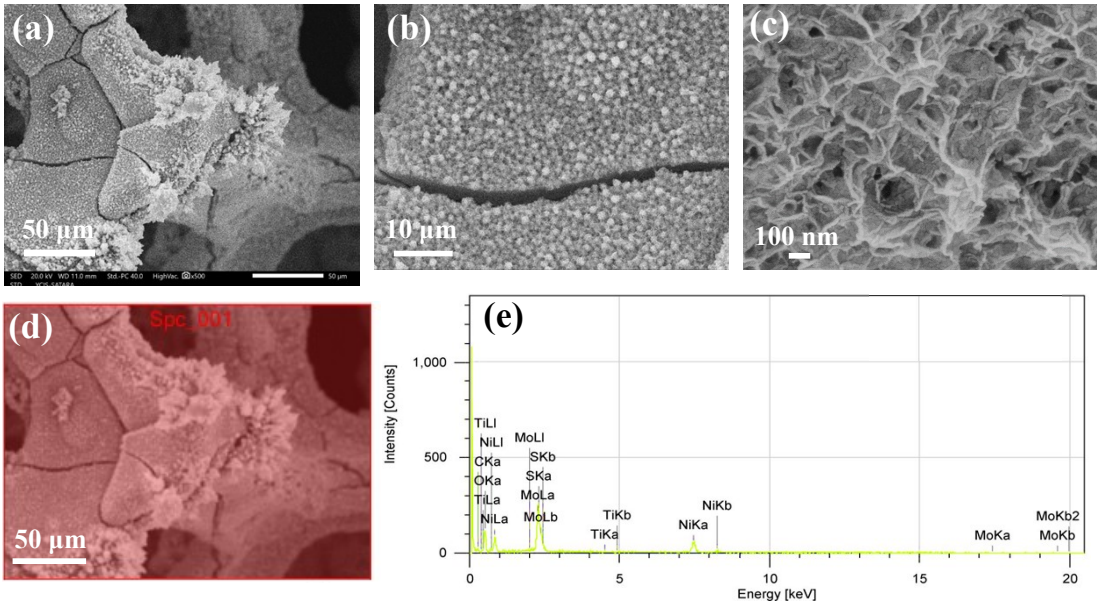

Fig. S5. (a-c) FESEM images of Ni_3S_2/MoS_2@MXene/NF hybrid electrode at different magnifications, showing a uniformly interconnected nanosheet architecture anchored on the MXene surface. (d) FESEM image showing the selected area used for EDX analysis. (e) EDX spectrum confirming the presence of Ni, Mo, S, Ti and C elements, consistent with the formation of the Ni_3S_2/MoS_2@MXene/NF hybrid structure.

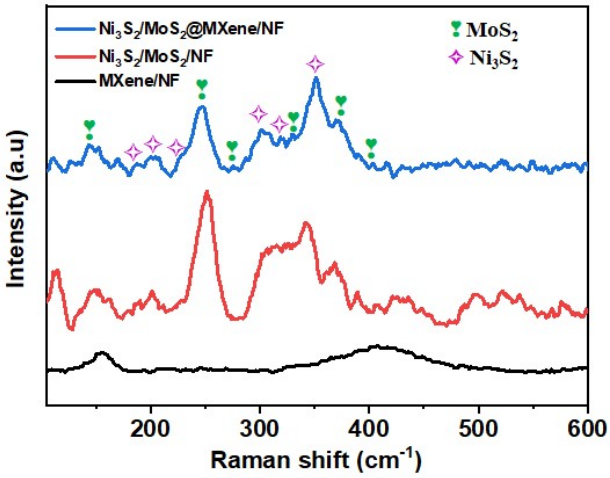

Fig. S6. Raman spectra of MXene/NF, Ni_3S_2/MoS_2/NF, and Ni_3S_2/MoS_2@MXene/NF.

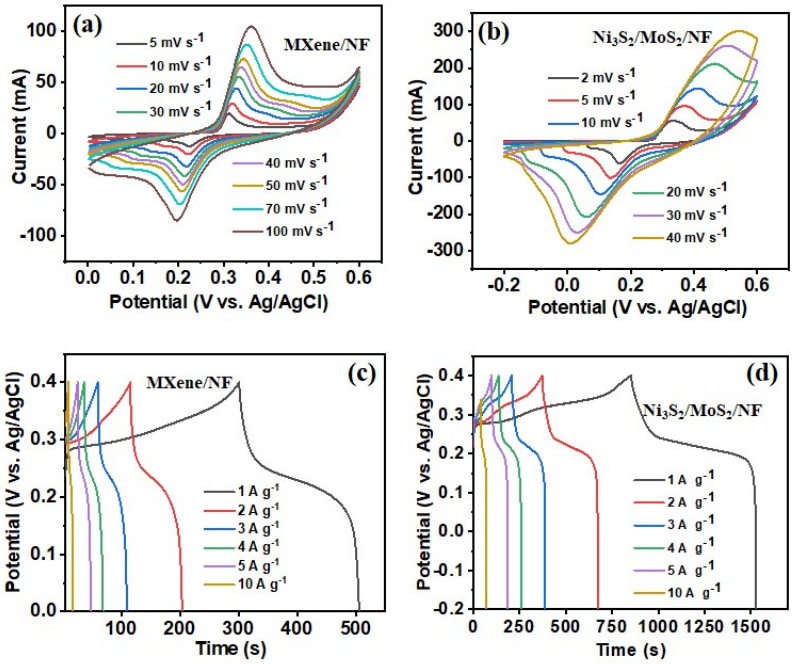

Fig. S7. (a, b) CV curves at different scan rate and (c, d) GCD curves at different current densities of MXene/NF and Ni_3S_2/MoS_2/NF, respectively.

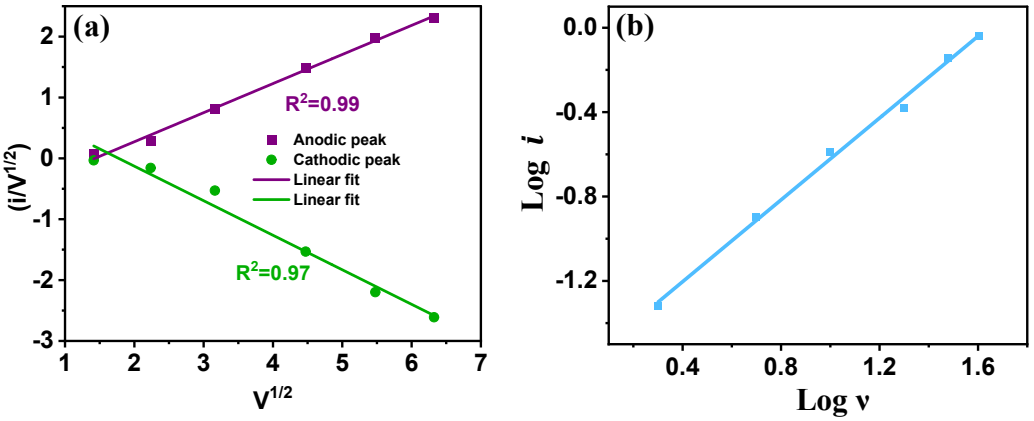

Fig. S8. Electrochemical characterization of Ni_3S_2/MoS_2@MXene/NF: (a) determination of b value and (b) calculation of k_1 and k_2.

Scan rate (v)	Charge separation (ΔEp)	Current ratio (ip)	Diffusion coefficient (D)
2	0.146	1	7.67755×10^{-11}
5	0.203	1.09	3.64868×10^{-11}
10	0.265	1.02	1.59755×10^{-11}
20	0.3403	1.03	8.14512×10^{-12}
30	0.4098	1.05	5.643×10^{-12}

Table S1: Calculation of diffusion coefficient (D) for Ni_3S_2/MoS_2@MXene/NF in 3M KOH

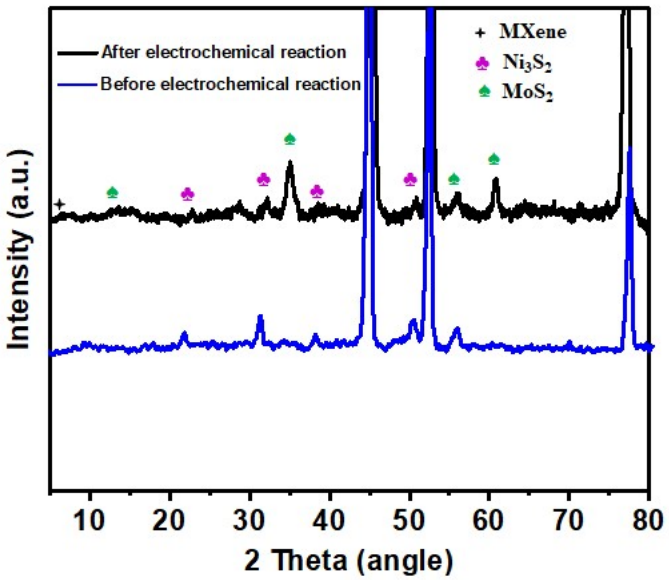

Fig. S9 XRD patterns of the Ni_3S_2/MoS_2@MXene/NF electrode before and after electrochemical cycling.

Table S2: Comparison of reported specific capacitance values of various electrode materials from the literature, alongside the specific capacitance achieved in this work.

Electrode material	Electrolyte	Specific capacitance	Ref
NiS_2/MoS_2 on Nickel foam	2 M KOH	4.46 F cm^2 at 5 mA cm^2	3
NiS_2@MoS_2	6 M KOH	848.2 C g^{-1} at 1 A g^{-1}	4
NiS_2/MoS_2@rGO	6 M KOH	645.3 F g^{-1} at 0.5 A g^{-1}	5
graphene/NiS_2	6 M KOH	478.1 F g^{-1} at 0.5 A g^{-1}	6.
MoS_2-graphene	1 M Na_2SO_4	243.0 F g^{-1} at 1 A g^{-1}	7
Hy-1T MoS_2@Cu_2S	2M KOH	1118 F g^{-1} at 1 A g^{-1}	8
MoS_2 nanowires	1 M KOH	244.0 F g^{-1} at 1 A g^{-1}	9
NiO/NiS	3 M KOH	1386.7 F·g^{-1} at 1 A g^{-1}	10
MoS_2/MoO_2@CNT	1 M KOH	228.4 F g^{-1} at 0.5 A g^{-1}	11
Fe_2O_3/MoS_2	3M KOH	266 F g^{-1} at 0.5 A g^{-1}	12

MoS_2 nanosheets on Mo foil	1M Na2SO4	192.7 F g^{-1} at 1 mA cm^{-2}	13
Ni_3S_2/MoS_2/NF	3M KOH	341.7 C g^{-1} at 1 A g^{-1}	14
Ni_3S_2@MoS_2	2M KOH	848 F g^{-1} at 5 A g^{-1}	15
1T/2H-MoS_2@$Ti_3C_2T_x$	2 M KOH	1162.22 F g^{-1} at 1 A g^{-1}	1
Co_4S_3/Ni_3S_2@MoS_2	1M KOH	1238 F g^{-1} at 1 A g^{-1}	16
Ni_3S_2@MoS_2/NF	6M KOH	12.6 F cm^{-2} at 10 mA cm^{-2}	17
Ni_3S_2/MoS_2@MXene/NF	3 M KOH	2310.0 F g^{-1} at 1 A g^{-1}	This Work

Table S3: Values of charge-transfer resistance and solution resistance for the investigated electrode materials.

Electrode material	Rct (Ω)	Rs (Ω)
Ti_3C_2/NF	1.446	0.382
Ni_3S_2/MoS_2/NF	62.59	0.688
Ni_3S_2/MoS_2@Ti_3C_2/NF	0.277	0.035

Table S4: Comparison of reported energy and power density values of various supercapacitor systems with those obtained in this study.

Electrode material	Energy and Power density	Ref
Ni_3S_2/MoS_2@NF-9//RGO	26.9 Wh kg^{-1} at 375 W kg^{-1}	14
NiS2@MoS_2//AC	37.2 Wh kg^{-1} at 0.8 kW kg^{-1}	4
1T/2H-MoS_2@$Ti_3C_2T_x$//AC	22.22 Wh kg^{-1} at 2880 W kg^{-1}	1
NiMoS4//AC	35 Wh kg^{-1} at 400 W kg^{-1}	18
s-MoS_2//CNS	7.4 W h kg^{-1} at 3700 W kg^{-1}	19
$CuCo_2O_4$//AC	18 Wh kg^{-1} at 259 W kg^{-1}	20
Ni_3S_2@PPy//AC	17.54 Wh kg^{-1}at 179.33 W kg^{-1}	21
Cu_2S/MoS_2@CM@rGO//AC	36.9 Wh kg^{-1} at 981.8 W kg^{-1}	22
MoS_2@CdS@GO//AC	40.69 Wh kg^{-1} at 700 W kg^{-1}	23

RNMS-36//rGO	32.8 Wh kg^{-1} at 373.7 W kg^{-1}	[24]
Ni3S2/MWCNT-NC//AC	19.8 Wh kg^{-1} at 798 W kg^{-1}	[25]
MXene-$NiCo_2S_4$//AC	27.24 Wh kg^{-1} at 480 W kg^{-1}	[26]
1T-MoS_2/$Ti_3C_2T_z$	12 Wh kg^{-1} at 139.9 W kg^{-1}	[27]
o-Ni_3S_2/Ti_3C_2/NF	30.4 Wh kg^{-1} at 800 W kg^{-1}	[28]
Ni_3S_2@NF//AC@NF	32 Wh kg^{-1} at 210.8 W kg^{-1}	[29]
rGO/Ni_3S_2(rGO)/PP-PEFs//rGO/Ni/PP-PEFs	29.1 Wh kg^{-1} at 390 W kg^{-1}	[30]
Ni_3S_2/MoS_2@MXene/NF//AC	46.66 Wh kg^{-1} at 2880 W kg^{-1}	This work

References

1 M. Patel, K. Mahabari, R. Patel, R. Mohili, A. A. Abdel Hafez, M. Govindasamy and N. K. Chaudhari, *ACS Appl. Energy Mater.*, 2025, **8**, 12684–12694.

2 X. Wang, H. Li, H. Li, S. Lin, W. Ding, X. Zhu, Z. Sheng, H. Wang, X. Zhu and Y. Sun, *Adv. Funct. Mater.*, 2020, **30**, 0190302.

3 Y. Liu, J. Sun, S. Lin, Z. Xu and L. Li, *J. Alloys Compd.*, 2020, **820**, 153113.

4 S. Hou, Y. Lian, Z. Xu, D. Wang, C. Ban, J. Zhao and H. Zhang, *Electrochim. Acta*, 2020, **330**, 135208.

5 J. Yuan, L. Jiang, J. Che, G. He and H. Chen, *ACS Appl. Nano Mater.*, 2021, **4**, 6093–6102.

6 X. Li, J. Shen, N. Li and M. Ye, *Mater. Lett.*, 2015, **139**, 81–85.

7 K. J. Huang, L. Wang, Y. J. Liu, Y. M. Liu, H. B. Wang, T. Gan and L. L. Wang, *Int. J. Hydrogen Energy*, 2013, **38**, 14027–14034.

8 A. Das, A. Paul, A. Mondal, K. Pal and B. B. Khatua, *J. Mater. Chem. A*, 2025, **13**, 24727–24740.

9 M. Manuraj, K. V. Kavya Nair, K. N. N. Unni and R. B. Rakhi, *J. Alloys Compd.*, 2020, **819**, 152963.

10 S. Y. Kim, C. V. V. M. Gopi, A. E. Reddy and H. J. Kim, *New J. Chem.*, 2018, **42**, 5309–5313.

11 Y. Tian, H. Du, M. Zhang, Y. Zheng, Q. Guo, H. Zhang, J. Luo and X. Zhang, *J. Mater. Chem. C*, 2019, **7**, 9545–9555.

12 X. Yang, H. Sun, L. Zhang, L. Zhao, J. Lian and Q. Jiang, *Sci. Reports,* 2016, **6**, 31591-.

13 K. Krishnamoorthy, G. K. Veerasubramani, P. Pazhamalai and S. J. Kim, *Electrochim. Acta*, 2016, **190**, 305–312.

14 J. Zhang, Z. Yao, M. Fan, H. Shen and T. Ma, *Ionics,* 2023, **29**, 2043–2052.

15 J. Wang, D. Chao, J. Liu, L. Li, L. Lai, J. Lin and Z. Shen, *Nano Energy*, 2014, **7**, 151–160.

16 C. Qu, J. Cao, Y. Chen, M. Wei, H. Fan, X. Liu, X. Li, Q. Wu, B. Feng and L. Yang, *Int. J. Hydrogen Energy*, 2023, **48**, 648–661.

17 T. Han, G. Guo, Y. Wei, Y. Zhang and Y. Sun, *Int. J. Electrochem. Sci.*, 2018, **13**, 10539–10547.

18 D. Du, R. Lan, J. Humphreys, W. Xu, K. Xie, H. Wang and S. Tao, *J. Electrochem. Soc.*, 2017, **164**, A2881.

19 T. N. Y. Khawula, K. Raju, P. J. Franklyn, I. Sigalas and K. I. Ozoemena, *J. Mater. Chem. A*, 2016, **4**, 6411–6425.

20 A. Shanmugavani and R. K. Selvan, *Electrochim. Acta*, 2016, **188**, 852–862.

21 L. Long, Y. Yao, M. Yan, H. Wang, G. Zhang, M. Kong, L. Yang, X. Liao, G. Yin and Z. Huang, *J. Mater. Sci. 2016 527*, 2016, **52**, 3642–3656.

22 H. Xu, Y. Zhang, F. Liu, Z. Yang, J. Xu and J. Liu, *ACS Appl. Nano Mater.*, 2024, **7**, 21340–21350.

23 S. Irfan, M. Aalim, M. H. Flaifel, I. Nazir, M. A. Shah, M. Q. Lone, A. Firdous, A. H. Pandith and G. N. Dar, *J. Energy Storage*, 2025, **106**, 114788.

24 W. Wei, B. Liu, Y. Gan, H. Ma, D. Chen, J. Qi and S. Li, *Surf. Coatings Technol.*, 2020, **403**, 126442.

25 C. S. Dai, P. Y. Chien, J. Y. Lin, S. W. Chou, W. K. Wu, P. H. Li, K. Y. Wu and T. W. Lin, *ACS Appl. Mater. Interfaces*, 2013, **5**, 12168–12174.

26 H. Li, X. Chen, E. Zalnezhad, K. N. Hui, K. S. Hui and M. J. Ko, *J. Ind. Eng. Chem.*, 2020, **82**, 309–316.

27 X. Yin, W. Zheng, H. Tang, P. Zhang and Z. M. Sun, *Nanoscale*, 2023, **15**, 10437–10446.

28 M. Tang, J. Shen, T. Zeng, L. Luo, L. Wu, M. Chen, S. Fu and L. Pu, *J. Solid State Electrochem.*, 2023, **27**, 2533–2543.

29 M. Shen, J. Liu, T. Liu, C. Yang, Y. He, Z. Li, J. Li and D. Qian, *J. Power Sources*, 2020, **448**, 227408.

30 N. Wang, G. Han, Y. Chang, W. Hou, Y. Xiao and H. Li, *Electrochim. Acta*, 2019, **317**, 322–332.